Reduced Order Modeling for Thermal Simulations of Electric Components with Surface-to-Surface Radiation

Matteo Zorzetto, Riccardo Torchio, Francesco Lucchini, Stefano Massei, Leonardo Robol, Fabrizio Dughiero

***Abstract*—This paper introduces the application of a reduced-order modeling technique for accurate temperature monitoring in Power Electronics modules. The methodology involves coupling the Finite Element Method with the radiosity equation to obtain high-fidelity models. These models account also for surface-to-surface radiation, an aspect that can have a high impact when the operating temperatures increase, and the components are close to each other. The Discrete Empirical Interpolation Method is employed to reduce the computation time with a limited effect on the accuracy of the prediction. Numerical and experimental results demonstrate the approach's effectiveness, showcasing high accuracy with minimal computation time and memory cost.**

***Index Terms*—Radiative heat transfer, model order reduction (MOR), Finite Element Method (FEM), discrete empirical interpolation method (DEIM).**

I. Introduction

THE increase in power density, along with the desire to have small-sized components, has led to increased compactness of Power Electronics (PE) modules. This means that several devices, some among them emitting heat, are near each other, typically within an enclosure. In PE converters, compactness is often achieved by increasing the switching frequency, thus reducing the dimensions of the passive components [1], and by packing them in close proximity [2]. Small-sized modules, with high power density (like the one seen in Fig. 1), require a high power heat dissipation, which may lead to dangerous hot spots [3], [4]. High operating temperatures and switching frequencies are typical of power modules made with wide-band-gap semiconductors like silicon carbide (SiC) [5], [6]. Developing thermal models for these high-power converters is crucial, given their application across various renewable technologies. These include serving as battery chargers for electric vehicles and trains, as well as inverters for photovoltaic (PV) systems [7].

M. Zorzetto, F. Lucchini, and F. Dughiero are with the Department of Industrial Engineering, Università degli Studi di Padova, Via Gradenigo 6/A, 35131 Padova, Italy (e-mail: matteo.zorzetto@studenti.unipd.it; francesco.lucchini@unipd.it; fabrizio.dughiero@unipd.it)

R. Torchio is with the Department of Industrial Engineering and the Department of Information Engineering, Università degli Studi di Padova, Via Gradenigo 6/A, 35131 Padova, Italy (e-mail: riccardo.torchio@unipd.it)

S. Massei and L. Robol are with the Department of Mathematics, University of Pisa, Pisa, Italy (e-mail: stefano.massei@unipi.it; leonardo.robol@unipi.it). The work of L. Robol has been supported by the National Research Center in High Performance Computing, Big Data and Quantum Computing (CN1 – Spoke 6). L. Robol and S. Massei acknowledge the MIUR Excellence Department Project awarded to the Department of Mathematics, University of Pisa, CUP I57G22000700001.

Indeed, having an accurate thermal model is important during the design and optimization of such components, where several time-consuming simulations must be done to check the reliability of the analyzed design, as the temperature is one of the main causes of failure in electronics [8].

Furthermore, accurate thermal models for PE components are crucial when implementing advanced control strategies, such as those rooted in Model Predictive Control (MPC) techniques [9]. These models can serve as soft sensors, providing virtual measurements of quantities that are challenging to probe [10], [11]. In this scenario, a computationally light model is desired, since real-time (or faster than real-time) simulations of the model are required [12].

When developing these models, the impact of thermal radiation is frequently disregarded due to its introduction of non-linearity, which consequently renders the problem more complex and challenging to resolve. This omission is justified when operating temperatures remain low since the portion of heat dissipated through radiation is insignificant compared to conduction and convection [13]. However, this is not the case for, e.g., high power density and compact module applications, where the operating temperature is high. For example, in an enclosure, heat dissipates from the component primarily through conduction and thermal radiation [14]. This is particularly true when airflow is restricted, hindering natural convection and thus making it ineffective for efficient device cooling [15]. In [14], Dallago and Venchi performed thermal simulations of a notebook that employed a fully passive thermal solution. When simulating the model without accounting for thermal radiation, the temperature of some components increased up to 56% [14].

It is noteworthy that, when radiation is considered, two phenomena exist: surface-to-ambient (s2a) radiation, where the components exchange heat by radiation toward the surrounding ambient with a presumed constant temperature, and surface-to-surface (s2s) radiation, where different parts of the components at different temperatures mutually exchange heat [16]. This latter phenomenon contributes to the heating of passive components placed in proximity to heat-dissipating ones.

Usually, because of their simplicity, thermal networks are adopted to model PE components. However, in general, thermal networks only allow for low-resolution temperature monitoring [3], [17]. More accurate thermal networks can be synthesized from models created using the Finite Element Method (FEM). These networks increase the accuracy but

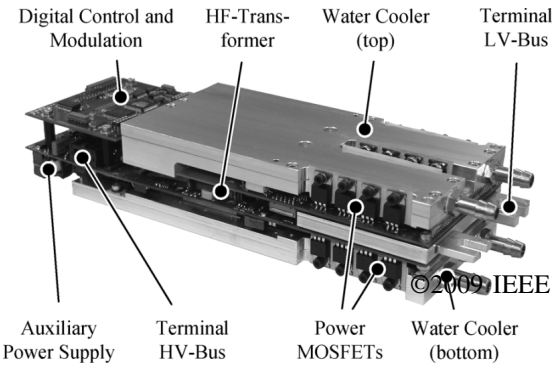

Fig. 1: High-Current Dual Active Bridge Converter for an Automotive Application [28].

also the computation time, and thus may require Model Order Reduction (MOR) techniques to reduce their complexity [18]–[21].

Coupling the FEM with thermal radiation provides an accurate but computationally expensive representation of the phenomena. In particular, including s2a thermal radiation makes the problem non-linear, and including s2s radiation requires generating, storing, and operating with dense matrices representing the non-local heat exchange between different parts of the component, thus significantly increasing the computational burden of the model [22], [23].

Some techniques have already been proposed to reduce the computational cost and memory requirements associated with incorporating s2s radiation in FEM models [23]–[25]. These methods work by refining the mesh or by partitioning the dense matrix needed for computations into blocks. This operation may be incompatible with real-time computations on inexpensive hardware due to the memory and complexity needed to operate with blocks.

In this paper, to tackle this problem, we employ the Proper Orthogonal Decomposition (POD) coupled with the Discrete Empirical Interpolation Method (DEIM) [26] to construct accurate and computationally light Reduced Order Models (ROMs) of PE components, including all radiation effects. A tailored version of the DEIM approach is employed with the interpolation node selection based on the column pivoted QR factorization [27]. The method is used to reduce the dimensions of the nonlinear system of equations, by combining projection and interpolation, employing snapshots (i.e., temperature maps of the model), to build a basis that is used to project, and thus reduce, the original model.

The remainder of the paper is structured as follows. First, a summary of surface-to-surface radiation, and its estimation using the radiosity method is presented in Section II. Section III discusses the approach used to reduce the order of the model. After that, in Section IV, the method is employed on a simple DC-DC converter (reported in Fig. 4) to show that even for a simple device, radiation may be relevant, and to prove the effectiveness of the reduction strategy. Finally, the main conclusion of this paper is drawn in Section V.

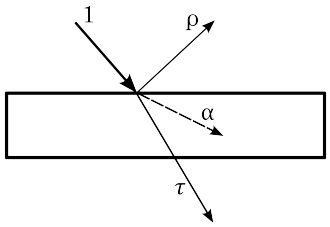

Fig. 2: Reflected, transmitted, and absorbed components of radiation.

II. Formulation of the problem

A. Properties of radiative surfaces

When thermal radiation hits a surface, as shown in Fig. 2 it can either be absorbed, reflected, or transmitted. From [29], it follows that:

$$\rho + \alpha + \tau = 1, \tag{1}$$

where ρ, α, τ are the reflectivity, absorptivity, and transmissivity coefficients, respectively. These coefficients are related to the reflected, absorbed, and transmitted fractions of the incoming radiation, and their values are generally dependent on the direction of the incoming radiation and the wavelength. Additionally, the temperature of the surfaces plays a role, influencing the emitted blackbody radiation, which varies with both wavelength and temperature [29]. This variation is characterized by the Planck distribution, expressed by the equation:

$$E_{\lambda,b}(\lambda, T) = \frac{C_1}{\lambda^5 \left[\exp\left(\frac{C_2}{\lambda T}\right) - 1\right]}, \tag{2}$$

where:

$E_{\lambda,b}(\lambda, T)$ is the spectral emissive power
λ is the wavelength,
T is the absolute temperature of the black body,
C_1, C_2 are constants [29].

This behavior can be generally approximated by considering the *total hemispherical* approximation of the emissivity, reflectivity, and absorptivity, obtained by averaging the properties over wavelength and direction [29]. The surfaces are considered *diffuse* rather than *specular*, so they reflect light uniformly, which is a good approximation for rough surfaces [29]. For PE applications, we can restrict the problem to the case of opaque surfaces only, where $\tau = 0$, so we can derive the reflectivity ρ as:

$$\rho = 1 - \alpha. \tag{3}$$

The specific power emitted from a *blackbody* is related to the Stefan-Boltzmann constant and the temperature of the surface via $e = \epsilon \sigma T_s^4$, where ϵ is the emissivity of the surface, equal to 1 in the case of a *blackbody* and less than 1 for a *graybody*. *Kirchhoff's law* states that for each wavelength $\epsilon(\lambda) = \alpha(\lambda)$ [30]. In this work, we considered the *total*

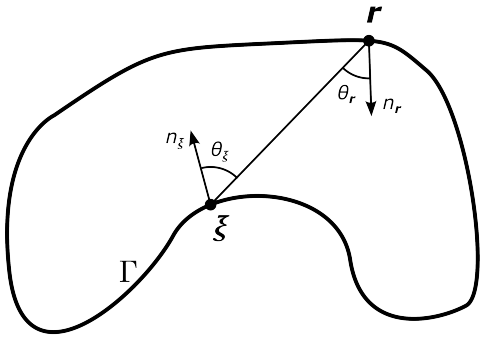

Fig. 3: Surface-to-surface radiation in an enclosure.

hemispherical approximations so we can write $\epsilon = \alpha$ and this lets us express the reflectivity as [29]:

$$\rho = 1 - \epsilon. \tag{4}$$

The openings of the enclosure are treated as surfaces at ambient temperature that do not reflect incoming radiation, resulting in an equivalent reflectivity equal to zero.

B. Continuous formulation of the radiosity equation

Under the assumption that each surface is a Lambertian diffuse reflector, the radiosity equation in an enclosure Γ is given by [31]:

$$u(\mathbf{r}) - \rho(\mathbf{r}) \int_\Gamma u(\boldsymbol{\xi}) G(\mathbf{r}, \boldsymbol{\xi}) V(\mathbf{r}, \boldsymbol{\xi}) d\boldsymbol{\xi} = e(\mathbf{r}), \qquad \mathbf{r}, \boldsymbol{\xi} \in \Gamma. \tag{5}$$

In (5), $u(\mathbf{r})$ represents the *radiosity*, i.e., the energy exiting from point $\mathbf{r}$. The second term of the equation is related to the energy coming from all other points $\boldsymbol{\xi}$ in Γ, reflected from $\mathbf{r}$. This reflected energy depends on:

- the visibility factor $V(\mathbf{r}, \boldsymbol{\xi})$, equal to 0 or 1, that determines if the two points *see* each other,
- the radiosity of point $\boldsymbol{\xi}$, i.e., $u(\boldsymbol{\xi})$,
- the reflection coefficient $\rho(\mathbf{r})$,
- the geometric relationship between points $\boldsymbol{r}$ and $\boldsymbol{\xi}$ $\mathcal{G}(\boldsymbol{r}, \boldsymbol{\xi})$ given by:

$$\begin{aligned} \mathcal{G}(\boldsymbol{r}, \boldsymbol{\xi}) &= \frac{(\boldsymbol{\xi} - \mathbf{r}) \cdot \mathbf{n}_\mathbf{r} (\boldsymbol{\xi} - \mathbf{r}) \cdot \mathbf{n}_\xi}{\pi ||\mathbf{r} - \boldsymbol{\xi}||^4} \\ &= \frac{\cos\theta_r \cos\theta_\xi}{\pi ||\boldsymbol{r} - \boldsymbol{\xi}||^2}. \end{aligned} \tag{6}$$

A graphical representation of geometrical quantities of (6) is given in Fig. 3. The right hand side of (5) represents the energy emitted from point $\boldsymbol{r}$, i.e., $e(\boldsymbol{r}) = \sigma\epsilon(\boldsymbol{r}) T_r^4$ [32].

C. Discrete formulation of the radiosity equation

To numerically solve (5), the boundary of the components must be discretized into boundary elements, such as triangles. In this paper, to provide a tool that can be seamlessly integrated with FEM software, we decided to use the same FEM mesh of the heat conduction problem. The discrete form factors are obtained by doing the integral average of (6) across each couple of surface patches i, j [31], obtaining:

$$F_{ij} = \frac{1}{A_i} \int_{A_i} \int_{A_j} \frac{\cos\theta_r \cos\theta_\xi}{\pi ||\boldsymbol{r} - \boldsymbol{\xi}||^2} V(\boldsymbol{r}, \boldsymbol{\xi}) dA_i dA_j. \tag{7}$$

F_{ij} represents the fraction of the radiation leaving the element i that reaches element j, and represents quantitatively *how much two surface elements see each other*. The form factor matrix $\boldsymbol{F} = \{F_{ij}\}$ was calculated by numerically integrating (7) for all $i < j$. The elements in the diagonal are zero, since the surface was discretized with flat triangles, and the other form factors were obtained through the reciprocity relation:

$$A_i F_{ij} = A_j F_{ji}, \tag{8}$$

where A_i represents the area of triangle i [29].

For large models, the form factor computation could be a bottleneck, and the *hemicube algorithm* [33] might provide a more efficient approximation. The visibility factors $V(\boldsymbol{r}, \boldsymbol{\xi})$, needed in (7) are instead obtained with an implementation of the Ray-Triangle intersection algorithm [34]. The quantity of interest is the net power flowing out of each surface triangle. We now proceed to discretize the radiosity equation (5), obtaining the vector $\boldsymbol{u}$ representing the outwards power of each triangle [25]:

$$(\mathbb{I} - (1 - \boldsymbol{\epsilon}) \boldsymbol{F})\, \boldsymbol{u} = \sigma \boldsymbol{\epsilon} \boldsymbol{T}^4, \tag{9}$$

where $\boldsymbol{\epsilon}$ represents the vector of the emissivity values of each triangle, which was used to replace the reflectivity in (5) thanks to (4). It should be noted that $\boldsymbol{T}^4$ in this case represents the element-wise fourth power of vector $\boldsymbol{T}$, containing the temperature of each surface element. We can then obtain the net power flowing out of each surface triangle $\boldsymbol{q}_{\text{net}}$. For triangle i, this is the power flowing out from i, minus the sum of the power that flows out of each triangle j which is intercepted by i, and can be represented by the following matrix equation [25]:

$$\boldsymbol{q}_{\text{net}} = (\mathbb{I} - \boldsymbol{F}) \left[\mathbb{I} - (1 - \boldsymbol{\epsilon}) \boldsymbol{F}\right]^{-1} \sigma \boldsymbol{\epsilon} \boldsymbol{T}^4 = \boldsymbol{D} \boldsymbol{T}^4. \tag{10}$$

D. Coupling radiosity with the heat conduction problem

To construct a model of the device under study, we used the FEM approach applied the heat conduction equation:

$$\text{In } \Omega: \quad \rho c \frac{\partial T}{\partial t} = \nabla \cdot (k \nabla T) + Q, \tag{11}$$

and coupled with the heat convection equation:

$$\text{On } \partial\Omega: \quad -k \frac{\partial T}{\partial n} = h(T - T_\infty). \tag{12}$$

If thermal radiation is not considered, the FEM model is given by:

$$\boldsymbol{M} \dot{\boldsymbol{x}} + (\boldsymbol{S} + \boldsymbol{H}) \boldsymbol{x} = \boldsymbol{q} + \boldsymbol{q}_{\text{conv}}. \tag{13}$$

where $\boldsymbol{M}, \boldsymbol{S} \in \mathbb{R}^{n \times n}$ are the mass and stiffness matrix, and $\boldsymbol{x} \in \mathbb{R}^n$ contains the temperature of each node of the mesh.

In (13), $\boldsymbol{H}$ and $\boldsymbol{q}_{\text{conv}}$ derive from the discretization of the convection boundary condition (12). Furthermore, $\boldsymbol{q}$ represents the internal heat generation of components subject to joule losses.

We now want to couple (13) with (10). The former is a relationship between nodal temperatures $\boldsymbol{x}$ and nodal heat fluxes $\boldsymbol{q} + \boldsymbol{q}_{\text{conv}}$. Instead, equation (10) takes as an input a vector containing the surface elements temperatures $\boldsymbol{T}$, and returns $\boldsymbol{q}_{\text{net}}$, i.e., the net heat flux due to radiation on each surface element. To couple surface-to-surface radiation with (13), we need to express it as a function of the nodal temperature, and the net heat flux should be mapped into nodes instead of surface elements. Matrix $\boldsymbol{N}$ is defined as the operator performing the average of the nodal temperatures, yielding the temperature of each triangle. The net radiation on each element is mapped on the nodes through matrix $\boldsymbol{B} = \{B_{li}\} = \int_{\Gamma_i} \phi_l d\Gamma_i$, where ϕ_l is the basis function of node l [32]. We can now express the radiation contribution in each mesh node using:

$$\boldsymbol{q}_{\text{rad}} = \boldsymbol{B}\boldsymbol{D}\boldsymbol{T}^4 = \boldsymbol{G}\boldsymbol{T}^4. \tag{14}$$

Combining the radiation boundary condition (14) with the original system of equations (13) returns the following system of nonlinear equations:

$$\boldsymbol{M}\dot{\boldsymbol{x}} + (\boldsymbol{S} + \boldsymbol{H})\boldsymbol{x} = \boldsymbol{q} + \boldsymbol{q}_{\text{conv}} + \boldsymbol{G}\left(\boldsymbol{N}\boldsymbol{x}\right)^4. \tag{15}$$

E. Solving the time-dependent problem

The FEM is described by local relationships between quantities, in particular, the temperature in a node of the mesh depends on the temperature of nearby ones. This provides a large, but sparse system of equations that describes the problem. Instead, the surface-to-surface radiation boundary condition defines a non-local coupling between all surface nodes. This makes matrix $\boldsymbol{G}$ dense, thus significantly increasing the computational burden. Dense matrix operations, combined with the fact that (15) is nonlinear in $\boldsymbol{x}$ make the problem expensive to solve, especially for time domain simulations.

One possibility is to solve for $\boldsymbol{x}$ the nonlinear problem (15) at each time step of the problem, but to reduce the computation time, we chose an approximate approach. Without considering the effect of thermal radiation, we discretized the resulting system using the Backward Euler Algorithm [35], approximating the solution at each step via:

$$\boldsymbol{x}_{k+1} \approx \boldsymbol{x}_k + \Delta t \boldsymbol{f}(\boldsymbol{x}_{k+1}, t_{k+1}), \tag{16}$$

where Δt is the time-step and $\boldsymbol{f}$ is obtained from (15) by algebraic manipulations.

The volumetric heat generation $\boldsymbol{q}$ and the convection boundary condition $\boldsymbol{q}_{\text{conv}}$, have been replaced with the product of an input matrix $\boldsymbol{P}$ times the input $\boldsymbol{u}$. Both the state vector and the input are functions of time.

Performing these operations, returned the following relationship:

$$\boldsymbol{E}_d\boldsymbol{x}_{k+1} = \boldsymbol{A}_d\boldsymbol{x}_k + \boldsymbol{B}_d\boldsymbol{u}_{k+1}, \tag{17}$$

where:

$$\boldsymbol{E}_d = \boldsymbol{M} + \Delta t(\boldsymbol{S} + \boldsymbol{H}) \tag{18}$$

$$\boldsymbol{A}_d = \boldsymbol{M} \tag{19}$$

$$\boldsymbol{B}_d = \Delta t \boldsymbol{P}. \tag{20}$$

Discretizing (15) using the Backward Euler method would require moving the nonlinear $\boldsymbol{G}(\boldsymbol{N}\boldsymbol{x})^4$ term to the left-hand side of (17), requiring the use of a nonlinear solver at each time step. For this reason, considering the slow evolution of the temperature w.r.t. the chosen time step, we opted for an approximated solution. The nonlinear term was calculated using the temperature distribution from the previous time step, obtaining the following equation:

$$\boldsymbol{E}_d\boldsymbol{x}_{k+1} = \boldsymbol{A}_d\boldsymbol{x}_k + \boldsymbol{B}_d\boldsymbol{u}_{k+1} + \boldsymbol{G}(\boldsymbol{N}\boldsymbol{x}_k)^4. \tag{21}$$

This approach was compared with the more accurate one (i.e., by actually solving the non-linear problem at each time step) on smaller problems but with similar dynamics. With the chosen time step, the two methods are comparable (i.e., discrepancies below 0.1 % were obtained).

III. Model order reduction

To reduce the cost of simulating (21) which is a high dimensional model, we look for a surrogate model with a much lower state dimension $r \ll n$. This is obtained using the POD, combined with the DEIM [26], [36] to handle the nonlinearity of the system. More precisely, we perform the following steps:

1) We run the Full Order Model (FOM) for s different combinations of inputs $\boldsymbol{u}$ and initial states. We collect the snapshot matrix $\tilde{\boldsymbol{V}} \in \mathbb{R}^{n \times n_T s}$ containing the solution of the FOM for all inputs and for each n_T timesteps. Analogously, we store the matrix $\tilde{\boldsymbol{W}} \in \mathbb{R}^{n_E \times n_T s}$ containing the quantities $(\boldsymbol{N}\boldsymbol{x}_k)^4$ where n_E is the number of elements in the finite element mesh.
2) We extract matrices $\boldsymbol{V}, \boldsymbol{W}$ with r and r_{DEIM} orthogonal columns spanning low-dimensional subspaces approximating the ranges of $\tilde{\boldsymbol{V}}, \tilde{\boldsymbol{W}}$, respectively. This can be either done with a truncated SVD for moderate n, or with a randomized rangefinder for larger problems [37]; the latter only requires matrix-vector multiplications of $\tilde{\boldsymbol{V}}$ and $\tilde{\boldsymbol{W}}$ with $\mathcal{O}(r + r_{\text{DEIM}})$ random vectors.

To obtain the reduced model, we approximate $\boldsymbol{x}(t) \approx \boldsymbol{V}\boldsymbol{x}^{(r)}(t)$ and impose a Galerkin condition, which yields the $r \times r$ nonlinear system; we discretize it by Backward Euler as we did for the FOM, obtaining:

$$\boldsymbol{E}_r\boldsymbol{x}_{k+1}^{(r)} = \boldsymbol{A}_r\boldsymbol{x}_k^{(r)} + \boldsymbol{B}_r\boldsymbol{u}_{k+1} + \boldsymbol{V}^T\boldsymbol{G}(\boldsymbol{N}\boldsymbol{V}\boldsymbol{x}_k^{(r)})^4, \tag{22}$$

where:

$$\boldsymbol{E}_r = \boldsymbol{V}^T\boldsymbol{E}_d\boldsymbol{V},\ \boldsymbol{A}_r = \boldsymbol{V}^T\boldsymbol{A}_d\boldsymbol{V},\ \boldsymbol{B}_r = \boldsymbol{V}^T\boldsymbol{B}_d.$$

Evaluating the nonlinear term $\boldsymbol{V}^T\boldsymbol{G}(\boldsymbol{N}\boldsymbol{V}\boldsymbol{x}_k^{(r)})^4$ would require assembling the full order solution. Hence, we further approximate it with a DEIM approach as:

$$(\boldsymbol{N}\boldsymbol{V}\boldsymbol{x}_k^{(r)})^4 \approx \boldsymbol{W}\boldsymbol{y}_k, \quad \boldsymbol{y}_k := (\boldsymbol{\Pi}^T\boldsymbol{W})^{-1}\left[\boldsymbol{\Pi}^T(\boldsymbol{N}\boldsymbol{V}\boldsymbol{x}_k^{(r)})^4\right],$$

where $\boldsymbol{\Pi}$ is a $n_E \times r_{\text{DEIM}}$ is a row-selection matrix (i.e, it contains r_{DEIM} columns of the $n_E \times n_E$ identity matrix). These columns can be chosen with well-established techniques that guarantee the invertibility of $\boldsymbol{\Pi}^T\boldsymbol{W}$; we use the one based on the pivoted QR decomposition proposed in [38]. Note that

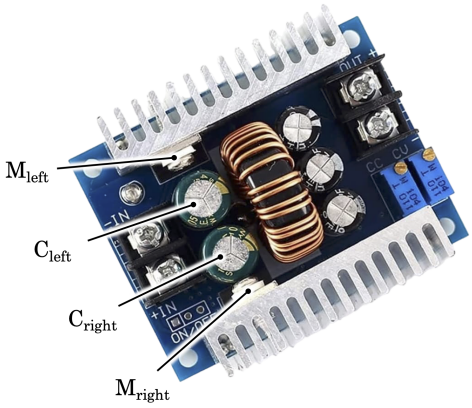

Fig. 4: Picture of the DC-DC converter with marked regions of interest.

TABLE I: Operating conditions of the power converter.

V_{in}	I_{in}	V_{out}	I_{out}
38.97V	2.97A	14.75V	7.21A

in view of the component-wise nature of the nonlinearity, we have $\boldsymbol{\Pi}^T(\boldsymbol{N}\boldsymbol{V}\boldsymbol{x}_k^{(r)})^4 = (\boldsymbol{\Pi}^T\boldsymbol{N}\boldsymbol{V}\boldsymbol{x}_k^{(r)})^4$. Substituting this approximation in (22) yields:

$$\boldsymbol{E}_r\boldsymbol{x}_{k+1}^{(r)} = \boldsymbol{A}_r\boldsymbol{x}_k^{(r)} + \boldsymbol{B}_r\boldsymbol{u}_{k+1} + \boldsymbol{G}_r(\boldsymbol{N}_r\boldsymbol{x}_k^{(r)})^4,$$

where the matrices:

$$\boldsymbol{G}_r := \boldsymbol{V}^T\boldsymbol{G}\boldsymbol{W}(\boldsymbol{\Pi}^T\boldsymbol{W})^{-1} \in \mathbb{R}^{r\times r_{\text{DEIM}}},$$
$$\boldsymbol{N}_r := \boldsymbol{\Pi}^T\boldsymbol{N}\boldsymbol{V} \in \mathbb{R}^{r_{\text{DEIM}}\times r}$$

can be computed once and for all in the offline phase. The reduced model is integrated with the same Backward Euler scheme with explicit nonlinearity used for the FOM. In this framework, computing each step of the ROM costs $\mathcal{O}(r(r + r_{\text{DEIM}}))$ flops, assuming that a Cholesky factorization of E_r is precomputed in the offline phase.

IV. Numerical Experiments

A. Preliminary analysis

To provide a realistic benchmark of the proposed approach, a DC-DC converter has been modeled using the Finite Element Analysis (FEA) software COMSOL Multiphysics®. The step-down converter used (see Fig. 4) can operate with an input voltage between $6-40$V and an output voltage of $1.5-30$V, the device is covered with a plastic lid to resemble an enclosure. The input was connected to a DC power supply and the output to a variable resistor. The setup used for the experiments can be seen in Fig. 5. Thermal pictures were taken with a Flir T420 thermal camera, and capacitors and heat sinks were covered with black electrical tape to provide the same value of surface emissivity. Fig. 6a was taken with the module in steady-state operating at the conditions seen in Table I. The unknown parameters of the numerical model were fit using temperature measurements taken with the thermal camera and the results were compared to the original as seen in Fig. 6b.

The FEA model is a simplification of the real device, considering heat generation in the components subject to losses, and heat conduction with radiation and convection boundary conditions. By disabling the surface-to-surface and surface-to-ambient boundary conditions, we can see in Fig. 6c that the temperature readings differ substantially from the ones obtained with the more accurate model. It should be noted that the thermal maps are presented all with the same scale of Fig. 6c for ease of comparison. This simple demonstration still shows that the effect of surface-to-surface radiation is significant even for this simple component. This can be verified quantitatively in Table II, where the measurements from the thermal camera are compared with the surface averaged temperatures in locations of interest, i.e., capacitors and MOSFETs shown in Fig. 4. Table II shows the impact of modeling surface-to-surface radiation on the average temperature of passive components. The temperature of the capacitors is greatly affected by the proximity of the coil and the MOSFETs, consequently, they change significantly if the s2s boundary condition is removed.

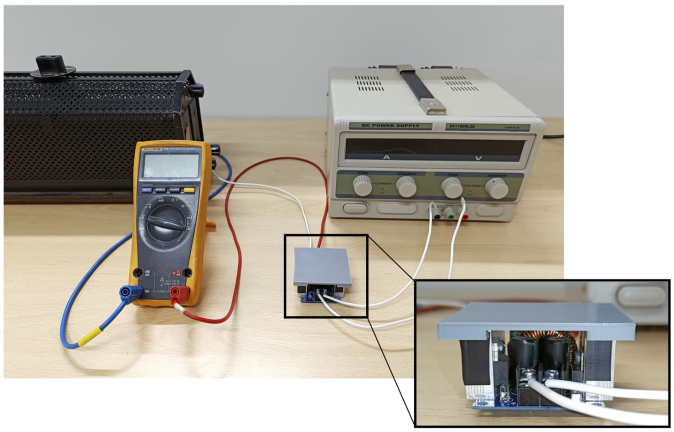

Fig. 5: Experimental setup.

TABLE II: Comparison between steady-state measurements and simulation of capacitors and MOSFETs surface temperatures °C.

	M_{left}	C_{left}	C_{right}	M_{right}
measurement	98.7	84.5	78.7	68.6
s2s+s2a	100.8	84.6	75.2	68.4
without radiation	112.6	98.7	85.2	73.5
only s2a	92.8	70.5	62.3	62.4

B. Model order reduction

The FEM model of the converter described in Section IV-A, was then constructed by using proprietary numerical tools developed in the MATLAB® environment. The resulting system has one input corresponding to the total dissipated power, which is then distributed in the heat-generating regions of the device. The outputs represent the average temperatures in volumes of interest of the device. The matrices needed for radiosity were built as explained in previous sections. In Fig. 7, the average temperature of the left capacitor (region 2 in Fig. 4) subject to the input power shown in Fig. 8 is depicted. The model is first simulated without radiation, then with both s2s and s2a, and finally by applying only

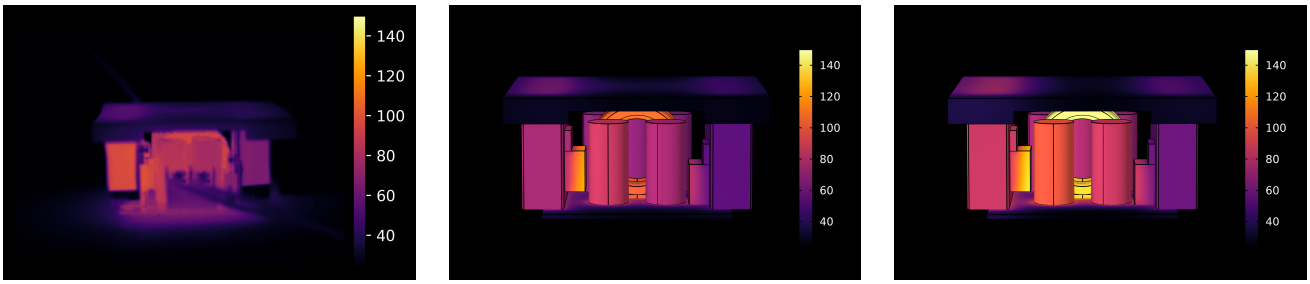

(a) Thermal image of the device under load.

(b) FEA simulation considering thermal radiation.

(c) FEA simulation ignoring thermal radiation.

Fig. 6: Comparison between measurements and FEA simulations. Color bar in °C.

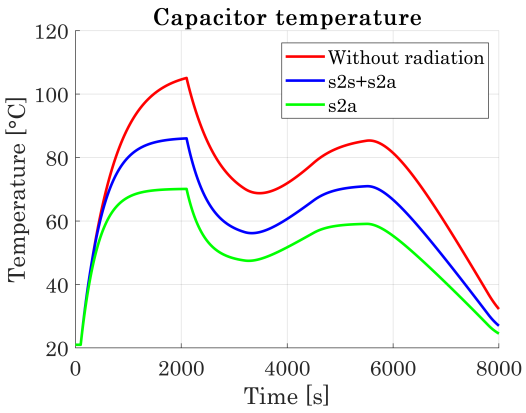

Fig. 7: Temperature estimate in the left capacitor with and without the contribution of thermal radiation.

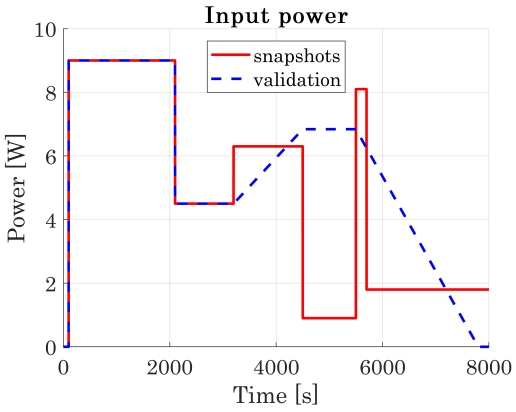

Fig. 8: Input power during snapshots collection and ROM validation.

the s2a boundary condition, considering the total visibility of the ambient for each radiating surface. Fig. 7 emphasizes the different trajectories taken by the temperature, further validating the impact of considering s2s radiation for this device.

To perform the MOR, snapshots must be computed, so the FOM was run using the series of steps of input powers shown in Fig. 8 with a time step of 1 second. Once the snapshots are collected, choosing the number of singular vectors for the

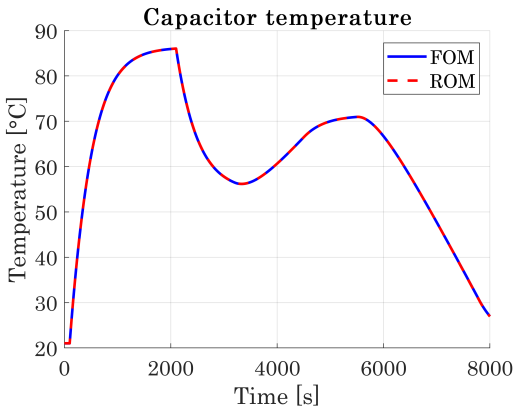

Fig. 9: Left capacitor temperature during validation.

TABLE III: Computation time and memory requirements comparison between full and reduced order model.

	n	s_{G}	Memory	ct
FOM	23619	23619×29515	5332 MB	1h 52min
ROM	7	7×6	3.23 kB	$0.61s$

POD and DEIM becomes a trade-off between model size and accuracy. To choose this value, the FOM and ROM were tested on new input data shown in Fig. 8.

The final ROM was built using 7 POD modes and 6 DEIM modes, the performance improvements reported here are also summarized in Table III. The number of states n was reduced from 23619 to 7. The size s_G of the radiation matrix $\boldsymbol{G}$ in (14) was reduced from 23619×29515 to 7×6. The computation time needed to run the simulation was reduced from 1 hr 52 min to less than 1 second, and the memory used to store the matrices was reduced from 5332 MB to less than 4 kB. The results obtained by the ROM were compared with the ones obtained by the FOM to test for loss of accuracy. The average temperature of the right capacitor is the quantity that showed the greatest maximum deviation from the FOM during the simulation. The quality is considered acceptable as this value is below 0.16°C.

V. Conclusion

A Proper Orthogonal Decomposition (POD) coupled with the Discrete Empirical Interpolation Method (DEIM) approach

has been applied to reduce the computational complexity of the heat conduction problem coupled with the surface-to-ambient and surface-to-surface radiation boundary conditions [25], [27]. The same mesh used for the heat conduction discretization is adopted to build the matrices needed for surface-to-ambient and surface-to-surface radiation, and the resulting model is then reduced. Thanks to the POD-DEIM method, high-fidelity physics-based models, can be seamlessly transformed into accurate Reduced Order Models (ROMs). By using this technique, both the computation time and memory needed to store the model of the device are greatly reduced, while the prediction error of the reduced order model is negligible. Finally, further improvements can be also achieved by employing faster strategies to build the radiosity matrix, in particular the calculation of the visibility factor, the main bottleneck of the proposed method. More efficient techniques can also take advantage of programmable graphics hardware to accelerate computations [33]. Starting from the proposed tool, future works will consider the applications of such ROMs for real-time control strategies and monitoring of electric components.

REFERENCES

[1] A. Stippich, C. H. Van Der Broeck, A. Sewergin, A. H. Wienhausen, M. Neubert, P. Schülting, S. Taraborrelli, H. van Hoek, and R. W. De Doncker, "Key components of modular propulsion systems for next generation electric vehicles," *CPSS Transactions on Power Electronics and Applications*, vol. 2, no. 4, pp. 249–258, Dec. 2017.

[2] S. Yano, Y. Nakayama, H. Kobayashi, S. Hiramatsu, M. Yoshida, K. Onda, K. Hayashi, and K. Yamazaki, "Development of compact power control unit for HEVs," in *2017 IEEE Energy Conversion Congress and Exposition (ECCE)*, Oct. 2017, pp. 584–588.

[3] E. Laloya, Ó. Lucía, H. Sarnago, and J. M. Burdío, "Heat Management in Power Converters: From State of the Art to Future Ultrahigh Efficiency Systems," *IEEE Transactions on Power Electronics*, vol. 31, no. 11, pp. 7896–7908, Nov. 2016.

[4] S. Jones-Jackson, R. Rodriguez, Y. Yang, L. Lopera, and A. Emadi, "Overview of Current Thermal Management of Automotive Power Electronics for Traction Purposes and Future Directions," *IEEE Transactions on Transportation Electrification*, vol. 8, no. 2, pp. 2412–2428, Jun. 2022.

[5] L. Han, L. Liang, Y. Kang, and Y. Qiu, "A review of SiC IGBT: Models, fabrications, characteristics, and applications," *IEEE Transactions on Power Electronics*, vol. 36, no. 2, pp. 2080–2093, 2021.

[6] A. Bindra, "Wide-Bandgap-Based Power Devices: Reshaping the power electronics landscape," *IEEE Power Electronics Magazine*, vol. 2, no. 1, pp. 42–47, Mar. 2015.

[7] G. Iannaccone, C. Sbrana, I. Morelli, and S. Strangio, "Power Electronics Based on Wide-Bandgap Semiconductors: Opportunities and Challenges," *IEEE Access*, vol. 9, pp. 139 446–139 456, 2021.

[8] S. S. Anandan and V. Ramalingam, "Thermal management of electronics: A review of literature," *Thermal Science*, vol. 12, no. 2, pp. 5–26, 2008.

[9] S. Vazquez, J. Rodriguez, M. Rivera, L. G. Franquelo, and M. Norambuena, "Model Predictive Control for Power Converters and Drives: Advances and Trends," *IEEE Transactions on Industrial Electronics*, vol. 64, no. 2, pp. 935–947, Feb. 2017.

[10] N. Baker, M. Liserre, L. Dupont, and Y. Avenas, "Improved Reliability of Power Modules: A Review of Online Junction Temperature Measurement Methods," *IEEE Industrial Electronics Magazine*, vol. 8, no. 3, pp. 17–27, Sep. 2014.

[11] M. Musallam and C. M. Johnson, "Real-Time Compact Thermal Models for Health Management of Power Electronics," *IEEE Transactions on Power Electronics*, vol. 25, no. 6, pp. 1416–1425, Jun. 2010.

[12] C. H. van der Broeck, R. D. Lorenz, and R. W. De Doncker, "Monitoring 3-D Temperature Distributions and Device Losses in Power Electronic Modules," *IEEE Transactions on Power Electronics*, vol. 34, no. 8, pp. 7983–7995, Aug. 2019.

[13] F. F. Wang, "Electronics packaging simplified radiation heat transfer analysis method," in *The Ninth Intersociety Conference on Thermal and Thermomechanical Phenomena In Electronic Systems (IEEE Cat. No.04CH37543)*, vol. 1, Jun. 2004, pp. 613–617 Vol.1.

[14] E. Dallago and G. Venchi, "Thermal characterization of compact electronic systems: A portable PC as a study case," *IEEE Transactions on Power Electronics*, vol. 17, no. 2, pp. 187–195, Mar. 2002.

[15] E. Papanicolaou and S. Gopalakrishna, "Natural Convection in Shallow, Horizontal Air Layers Encountered in Electronic Cooling," *Journal of Electronic Packaging*, vol. 117, no. 4, pp. 307–316, Dec. 1995.

[16] R. Siegel, *Thermal Radiation Heat Transfer: Vol. 3: Radiation Transfer with Absorbing, Emitting, and Scattering Media*. Scientific and Technical Information Division, National Aeronautics and Space Administration, 1971.

[17] V. d'Alessandro and N. Rinaldi, "A critical review of thermal models for electro-thermal simulation," *Solid-State Electronics*, vol. 46, no. 4, pp. 487–496, Apr. 2002.

[18] A. S. Bahman, K. Ma, and F. Blaabjerg, "A Lumped Thermal Model Including Thermal Coupling and Thermal Boundary Conditions for High-Power IGBT Modules," *IEEE Transactions on Power Electronics*, vol. 33, no. 3, pp. 2518–2530, Mar. 2018.

[19] L. Codecasa, D. D'Amore, and P. Maffezzoni, "Compact modeling of electrical devices for electrothermal analysis," *IEEE Transactions on Circuits and Systems I: Fundamental Theory and Applications*, vol. 50, no. 4, pp. 465–476, Apr. 2003.

[20] L. Codecasa, V. d'Alessandro, A. Magnani, and A. Irace, "Circuit-Based Electrothermal Simulation of Power Devices by an Ultrafast Nonlinear MOR Approach," *IEEE Transactions on Power Electronics*, vol. 31, no. 8, pp. 5906–5916, Aug. 2016.

[21] L. Codecasa, D. D'Amore, and P. Maffezzoni, "Compact thermal networks for modeling packages," *IEEE Transactions on Components and Packaging Technologies*, vol. 27, no. 1, pp. 96–103, Mar. 2004.

[22] J. R. Gosselin and Q. Y. Chen, "A computational method for calculating heat transfer and airflow through a dual-airflow window," *Energy and Buildings*, vol. 40, no. 4, pp. 452–458, Jan. 2008.

[23] N. Qatanani and I. Alzeer, "On the fast matrix computation for the heat radiation integral equation," *International Journal of Mathematics and Computer Science*, vol. 1, no. 4, pp. 461–472, 2006.

[24] C. Scheiblich, V. Kolitsas, and W. Rucker, "Compression of the Radiative Heat Transfer BEM Matrix of an Inductive Heating System Using a Block-Oriented Wavelet Transform," *IEEE Transactions on Magnetics*, vol. 45, no. 3, pp. 1712–1715, Mar. 2009.

[25] A. Voigt and C. Weichmann, "Adaptive FEM/BEM Coupling for Solving Global Heat Transfer in High-Temperature Furnaces," *Numerical Heat Transfer, Part B: Fundamentals*, vol. 51, no. 1, pp. 25–41, Jan. 2007.

[26] S. Chaturantabut and D. C. Sorensen, "Nonlinear Model Reduction via Discrete Empirical Interpolation," *SIAM Journal on Scientific Computing*, vol. 32, no. 5, pp. 2737–2764, Jan. 2010.

[27] Z. Drmač and S. Gugercin, "A New Selection Operator for the Discrete Empirical Interpolation Method—Improved A Priori Error Bound and Extensions," *SIAM Journal on Scientific Computing*, vol. 38, no. 2, pp. A631–A648, Jan. 2016.

[28] F. Krismer and J. W. Kolar, "Accurate Power Loss Model Derivation of a High-Current Dual Active Bridge Converter for an Automotive Application," *IEEE Transactions on Industrial Electronics*, vol. 57, no. 3, pp. 881–891, Mar. 2010.

[29] T. L. Bergman, F. P. Incropera, A. S. Lavine, and D. P. Dewitt, *Fundamentals of Heat and Mass Transfer*, 7th ed. Hoboken, NJ: Wiley, 2011.

[30] F. Kelly, "On kirchhoff's law and its generalized application to absorption andemission by cavities," in *2nd Aerospace Sciences Meeting*, 1965, p. 135.

[31] A. Voigt, N. Hanssen, and C. Weichmann, "The radiosity equation for solving global heat transfer in industrial furnaces," *Mathematical and Computer Modelling*, vol. 39, no. 2, pp. 145–150, Jan. 2004.

[32] C. Weichmann, R. Backofen, and A. Voigt, "Time dependent 3D heat radiation calculation in high temperature furnaces," *WIT Transactions on Engineering Sciences*, vol. 46, 2004.

[33] S. Kramer, R. Gritzki, A. Perschk, M. Rösler, and C. Felsmann, "Numerical simulation of radiative heat transfer in indoor environments on programmable graphics hardware," *International Journal of Thermal Sciences*, vol. 96, pp. 345–354, Oct. 2015.

[34] T. Möller and B. Trumbore, "Fast, Minimum Storage Ray-Triangle Intersection," *Journal of Graphics Tools*, vol. 2, no. 1, pp. 21–28, Jan. 1997.

[35] C. Vuik, F. Vermolen, M. Van Gijzen, and M. Vuik, *Numerical Methods for Ordinary Differential Equations*. TU Delft Open, 2023.

[36] M. Barrault, Y. Maday, N. C. Nguyen, and A. T. Patera, "An 'empirical interpolation'method: application to efficient reduced-basis discretization of partial differential equations," *Comptes Rendus Mathematique*, vol. 339, no. 9, pp. 667–672, 2004.
[37] N. Halko, P.-G. Martinsson, and J. A. Tropp, "Finding structure with randomness: Probabilistic algorithms for constructing approximate matrix decompositions," *SIAM review*, vol. 53, no. 2, pp. 217–288, 2011.
[38] Z. Drmac and S. Gugercin, "A new selection operator for the discrete empirical interpolation method—improved a priori error bound and extensions," *SIAM Journal on Scientific Computing*, vol. 38, no. 2, pp. A631–A648, 2016.